Solid state dual electrode electroanalysis under hydrodynamic conditions: Application to pH-controlled in-line sensing.

Keywords: Microfluidics, 3D-printed, COMSOL, Electrochemical Detection, Electrochemical pH control, generator-collector, dual electrode, ultramicro interdigitated electrode array

Authors: Shane O'Sullivan, Fernando Diaz, Ian Seymour and Alan O'Riordan*

Nanotechnology Group, Tyndall National Institute – University College Cork, Cork, Ireland, T12 R5CP

alan.oriordan@tyndall.ie

Abstract

While electrochemically driven, pH control-enabled, dual electrode sensing under quiescent conditions is emerging as a viable electroanalytical method, application of this approach under hydrodynamic conditions is less well documented. In this work we report the development of a finite element model (COMSOL Multiphysics™) to simulate electrochemical pH control under both quiescent and hydrodynamic conditions. We used these simulations to elucidate the effect of flowrate on our pH control method. Adjustments to the applied currents were made so as to compensate for the removal of generated protons by hydrodynamic flow, thereby allowing effective pH control under different flow conditions. Once optimised, this approach was applied to the detection of hypochlorous acid under various flow rates. To this end, the sensitivity of the sensors benefitted from both the localized electrochemical pH control and the signal-boosting effect associated with hydrodynamic forces.

Introduction

Societal adoption of the Internet of Things (IoT) technologies has been both rapid and ubiquitous, with the number of devices predicted to be in use expected to reach more than 29 billion by 2030.[1] These technologies have wide-ranging applications, in both industrial and consumer market places. This rapid growth of the IoT market is driving the need for additional, more functional and reliable sensors that can operate and communicate on IoT networks. Sensor devices typically employ a variety of transducer methods such as optical, [2-4] electrical, [5-7] and/or microelectromechanical (MEMS)-based detection mechanisms. [8-10] However, optical and MEMS sensor devices require their transduced signals to be

converted from their original format into an electrical signal that can then be transmitted across a network. This requires additional circuitry adding cost in terms of components and an energy budget.

In contrast, electrochemical sensors provide a direct electrical read-out and, as such, are compatible and may be easily integrated into different IoT type networks. Electrochemical sensors possess many other benefits such as their low power requirements, high sensitivity, ease of use, miniaturisation, cost effectiveness, and portability making them ideal candidates for use in remote point of use sensing applications. [11-14] They have been applied to a wide range of target analytes including: heavy metals, [15-17] microorganisms, [18-20] pesticides, herbicides as well as agricultural nutrient runoff to name but a few. [21-24]

One potential application of portable electrochemical systems is for use in water quality analysis. Typically, sterilisation of drinking water involves the addition of chemical reagents, usually chlorinated species, to water as an oxidising species. However, if this disinfection dosage step is performed incorrectly, excess chlorine present in drinking water can lead to health complications such as bladder cancer and death, while insufficient concentration will not provide sufficient biocidal control.[25-28] As such, there is a need for facile accurate point of use detection 'in-line' or 'at-line'- for chlorine detection in water networks to ensure sufficient residual chlorine concentration at the distribution networks. Electrochemical sensors can provide a reliable and portable method for detection particularly when adapted to chlorine measurement. However, at present this analysis is limited in that it would require the addition of acids and/or buffer in order to protonate the hypochlorite chlorite ion to its protonated detectable form; which is pH dependent. [29-31] Recently Seymour, et al. [32] demonstrated a new method for chlorine sensing using electrochemical pH control, whereby a four electrode electrochemical sensor system comprising two interdigitated electrodes (IDE) employed as working electrodes. In this approach, one IDE was used as a sensor while the second IDE was utilised as a protonator electrode; used to control the pH of the test solution in the immediate vicinity of the sensor thereby eliminating the need to add chemical reagents. Although elegant, this approach has primarily been performed in static quiescent solutions to date with only few reports on hydrodynamic pH control published in the literature. [33]

Electrochemical sensors and systems have been utilised and simulated theoretically throughout the years, [32, 34-37] however, the majority of this work has been undertaken using quiescent conditions. Incorporation of flow has long been understood to boost electrochemical sensor responses by replenishing oxidised/reduced analyte at a sensor surface.[38-41] The addition of convection, as an additional mode of mass transport, in combination with Fickian diffusion, facilitates more rapid delivery of an analyte to a sensor surface; leading to more analyte molecules/ions in contact with a sensor surface over a set timeframe. Furthermore, convection also effectively removes oxidised / reduced analyte from a sensor surface. Both these traits lead to the diffusion limitations, commonly observed in quiescent systems, being surmounted. Consequently, the use of fluid flow combined with electrochemical sensors is an interesting area of research. Most commonly, the incorporation of fluid flow, hydrodynamics, with electrochemical sensors has been achieved using a rotating ring-disk electrode set-up. [42-46] Incorporating microfluidic components on a chip surface is a growing area of research. Concerning the latter, the dominant method employs soft-lithography to define microfluidic elements, typically polydimethylsiloxane (PDMS). as first reported by Xia and Whitesides. [47] In this approach both the substrate and microfluidic element are oxygen plasma treated, to create Si-OH bonds on both surfaces, aligned and brought into conformal contact with each other such that covalent Si-O-Si bonds form between the two components through a condensation reaction. [39, 48 49-51] For example, Ko et al, amongst others, employed this method for carbon nanotube-based electrode sensors, patterned onto a polyethylene terephthalate surface. [39, 48] in that work, a PDMS microfluidic device was bonded to their substrate by treating both with O_2 plasma, bringing them into conformal contact overnight allowing covalent bonds to form. This approach works well with oxidised surfaces but is problematic when trying to attach to other dielectric surfaces, such as silicon nitride, due to the lack of oxygen atoms in the Si_3N_4 layer. Nitride is the preferred passivation layer for use with silicon chip based electrochemical sensors as it is a dense, non-porous layer and, as such, does not allow electrolyte molecules ingress into the layer thereby preventing unwanted parasitic capacitances. [52-53]

To this end, new microfluidic production methods, such as xurography [41, 54-55] and 3-D printing, [38, 56-61] are being explored by different research groups. [62-67] With advances in additive production capabilities, the use of micro-scale channels with electrochemical sensors has now become more facile with less fabrication expertise required compared to the photolithography driven microfabrication techniques previously employed. Often, designs require complex multi-step processes that can be time consuming, Swensen, et al. [68] requiring a multi-step process and the use of hazardous chemicals thereby restricting the approach to the laboratory settings. Progress has also been made in reducing the time required for microfluidic production, such as through the use of xurography as shown by Speller, et al. [69] however, these methods still require multi-step processes. Each step presents a potential source of error with alignment issues, and with human input required for several steps. 3D printing in particular, addresses the issues of microfluidic fabrication and integration with sensors, and also has the ability to produce multiple reproducible components in parallel.

In this work, we employ resin 3-D printing to rapidly create reliable and reusable microfluidic components and combine these with our silicon chip -based electrochemical sensor platform. [38, 56, 58] We minimise potential errors by automating the entire microfluidic production process and developed a single step process for alignment with the on-chip sensors. To understand the effect of flow on solid state electrodes operating in generator-collector mode (analogous to ring-disc systems) we undertake a finite element study on the application of electrochemical pH control under hydrodynamic systems. We then confirm this theoretical study experimentally and demonstrate its feasibility through pH dependent chlorine detection under these hydrodynamic conditions. An iterative feedback approach allowed the microfluidic elements to be tweaked and optimised. An additional advantage of the 3D-printed modular approach is reusability, i.e., it allows the system to be disassembled, cleaned and a new chip inserted as required. This is possible as the elements are not irreversibly covalently bonded to a chip surface (such as in soft-lithography) thereby increasing the sustainability of this approach. A commercial colorimetric free-chlorine detector was used to confirm results.

EXPERIMENTAL SECTION

Electrode Fabrication

Silicon chip based devices were fabricated as described by Dawson et al, [70]with the subsequent modifications proposed by Seymour et al [71] also included. Each sensor consisted of two combs of gold interdigitated ultramicroelectrodes, as working electrodes, as well as platinum pseudo reference and gold counter electrodes. Chips were designed with a peripheral microSD pinout to permit interfacing with external electronics via a microSD port. All devices were fabricated on 4-inch silicon wafers bearing a thermally grown 300 nm silicon dioxide layer. Blanket metal evaporation of Titanium (10 nm) and Gold (100 nm) (Temescal FC-2000 E-beam evaporator) and lift off technique to yield interdigitated microband comb structures. The first comb (WE1) had 33 tines, while the second comb two (WE2) had 34 tines. Each comb was 1 µm wide, 178 µm long, 100 nm high and had an inter-electrode gap of 2 µm. A second metal evaporation and subsequent lift-off step was undertaken to pattern the interconnection tracks, contact pads and the gold counter electrode (90 µm x 7mm). A third and final metal evaporation was performed to pattern the platinum pseudo reference electrode (90 µm x 7mm). Silicon nitride was then blanket deposited using plasma enhanced chemical vapour deposition across the whole wafer to act as an insulating layer. This insulating layer was used to prevent unwanted electrochemical interactions along the connection tracks. To allow electrolyte access to the ultramicroband electrodes, vias (windows) were opened in the insulating Si_3N_4 layer (above the sensor electrodes using photolithography and dry etching. Additional vias were opened over the counter and pseudo-reference electrodes as well as the periphery microSD contact pads. Each device contained three separate interdigitated electrode sensors which are separated by 1.88 mm. This separation was maintained to prevent cross talk, i.e., electrochemical reactions occurring at one sensor from interfering with a neighbouring sensor (when operating without the microfluidic component) and also to provide sufficient surface area between the electrodes to facilitate correct integration of the microfluidic channels to prevent leaking and cross talk. Following fabrication, the wafer was diced to produce 28 separate chip dice.

Microfluidic System

A 3D-printed modular microfluidics platform was designed to enable solutions to be flowed over electrode surfaces. This system, shown in greater detail in Figure 1, consisted of three components: a clear tough resin (Formlabs Inc clear resin) for both the top and bottom layers and a soft flexible resin (Formlabs Inc flexible 80a resin) for the middle 'gasket' layer. The microfluidics channels were defined in this flexible middle layer. All components were designed using Solidworks™ software. The designs were 3D-printed using a Formlabs Inc 3+ printer. Polytetrafluoroethylene (PTFE) tubing (Merck Life Science Ltd) with an outer diameter of 1.5 mm was connected to a stainless steel dispensing tip 20G (Merck Life Science Ltd) to and connected to the microfluidic channel. A 10 mL syringe (Sigma Aldrich) was filled with the solution being analysed and a digital programmable pump (NE-1000) allowed for liquid to be dispensed at controlled volumes and flowrates. The accuracy of this digital pump was confirmed by flowing a known volume of water into a pre-weighed beaker for a set amount of time and then measuring the mass increase and comparing against expected mass using a calibrated four-point balance (OHaus Pioneer PA213)

Electrode characterisation

Following fabrication, each chip was inspected using optical microscopy to identify any visible defects or faults and any defective chips discarded. Prior to electrochemical characterisation, chips were first cleaned by rinsing with acetone followed by de-ionized water. The chips were subsequently dried using nitrogen and inserted into a microfluidic holder. Electrochemical analysis was performed using an Autolab Bipotentiostat (MAC80150 with BA Module, Metrohm), within a Faraday cage. Cyclic voltammograms (CV) were performed in the voltage range of -0.15 V to 0.45 V at 50 mV/s at the first interdigitated comb (WE1) in 1 mM/L ferrocene carboxylic acid (FCA, Sigma Aldrich, 97%) while the second interdigitated comb of electrodes, (WE2) was biased at -0.15 V; for the duration of the scans. All electrochemical measurements were recorded versus the on-chip gold counter and platinum pseudo-reference electrodes in solutions at room temperature (~ 21 °C).

pH calibration of buffers in static and flow conditions

To accurately calibrate the pH control, an external Ag/AgCl reference was used. A beaker was placed downstream containing the external reference and filled with the appropriate buffer. The outlet tube for the microfluidic device was submerged in these buffer solutions to ensure a closed circuit. Chemically buffered solutions were prepared by mixing various ratios of citric acid monohydrate and monosodium phosphate (Sigma Aldrich). The pH of each solution was determined using a calibrated pH probe (Thermo Scientific Orion star A211 pH meter). A phosphate buffer (PB) solution was prepared using 268.8 mg sodium phosphate monobasic and 110.2 mg sodium phosphate dibasic, then making this solution up to 1 L using deionised water. This generated a pH 7.4 10 mM solution of PB, which was used for all electrochemical pH control buffer experiments where a potential window of -0.2V to 1.6V was used, with a scan rate of 50 mV, varying a potential bias at WE2 for the electrochemical pH control. All electrochemical measurements were recorded versus the on-chip gold counter and the external Ag/AgCl reference electrode, in solutions at room temperature (~ 21°C).

pH adjustment in water samples

Artificial drinking water (ADW) samples were prepared to simulate real drinking water conditions but without any residual chlorine present. ADW was prepared by dissolving 1 g of sodium bicarbonate, 0.0654 g of magnesium sulphate (Sigma Aldrich, 99.5% anhydrous), 0.3414 g calcium sulphate dehydrate (Honeywell, 99%), 0.007 g potassium phosphate dibasic (Fluka, 98%), potassium phosphate monobasic (Sigma Aldrich, 99%) and 0.01 g sodium nitrate (Sigma Aldrich, 99%) in 10 L of deionised water. For localised pH control, voltammograms were performed in ADW samples by scanning WE1 from -0.2 V to 1.2 V at 50 mV/s with WE2 biased at ~1.6 V to protonate (acidify) the local environment of the sensing electrodes via hydrolysis of water. The local pH can then be readily controlled by adjusting the applied potential to drive the appropriate current, as shown by O'Sullivan et al. [37] In acidic conditions, the pH can be changed through the water splitting reactions of Eqs. (1) and (2):

$$Cathode: 2H^+ + 2e^- \rightarrow H_2 \quad (1)$$

$$Anode: 2H_2O \rightarrow O_2 + 4H^+ + 4e^- \quad (2)$$

Diffusion simulations

Diffusion simulations of proton concentrations in the vicinity of the protonator electrodes (WE2) were performed using Fick's second law. A model was designed to simulate the generation of protons at the protonator electrodes, and their subsequent diffusion from these electrodes, using finite element analysis software, Comsol Multiphysics 6.0 ™, in line with the galvanostatic model shown previously. [37] The model boundary conditions were set at as a box 930 µm high by 5 mm wide, representing the experimental domain. Two sets of interdigitated 1 µm wide microband electrodes (34 protonator electrodes and 33 sensing electrodes), separated by 2 µm were defined at the bottom boundary layer. By fixing the anodic current to the protonator (WE1), a flux of protons was applied at the surface of the protonators, and the flux was assumed to be proportional to the current applied to the electrodes. The initial pH within the experimental domain was set to pH 7. The proton diffusion coefficient used for the simulation was 9.31×10^{-5} $cm^2 s^{-1}$. [72]

Once the initial static diffusion simulations were undertaken, the addition of a single-phase fluid flow was introduced into the model through the incorporation of the laminar flow module in Comsol ™. This step employed the incompressible flow form of the Navier-Stokes with Stokes flow included, as shown in Error! Reference source not found. below**.** The addition of convection as another form of mass transport was applied to the simulations. The effect of varying the flowrate, using the parametric sweep function, was investigated. The entrance length and thickness for the fluid flow were set to 500 µm. All other parameters remained unchanged from previous simulations.

$$\rho(u.\nabla)u = \nabla.[-\rho I + K] + F \qquad (3)$$

Where ρ is density of the fluid, K is the stress tensor, I is the identity matrix, u denotes the velocity field and F is the Faraday constant.

Detection of free-chlorine with pH control in the absence of flow

Based on the work of Seymour, et al. [32] the electrochemical pH control method based on oxygen evolution was employed to locally control the pH for chlorine analysis within a channel without any

fluid flow. This allowed electrochemical pH control of samples via the hydroylysis of water; leaving a net excess of protons. Similarly, the voltage at which the gold oxide reductive peak minimum occurred was used to approximate the local pH at a sensor. This approach was benchmarked against a set of know standards using a chemically controlled sample altered using different buffers. The targeted pH for chlorine detection was selected to be pH 3 as this was shown to be an area of high specificity for hypochlorous acid detection by Seymour, et al. [32] A fixed potential bias of 1.6V was applied to WE2 to drive the local pH down to 3. Initial scans were performed in a known concentrations of free-chlorine added to ADW, which was electrochemically acidified to pH 3, in order to establish the appropriate cyclic voltammetry parameters. Working chlorine samples were prepared by diluting Milton Sterilising Fluid (2% Sodium Hypochlorite) to the desired concentration. The concentration of free-chlorine in these samples were then measured and confirmed using a standard commercial free-chlorine colorimeter (Pocket Colorimeter II 58700-00 with CL_2 Test Kit), prior to electrochemical analysis. CV's were performed in the voltage range 0.85 V to -0.2 V (versus Pt pseudo-reference) at a 50 mV/s scan rate. All scans were repeated in quadruplet, with the first scan disregarded as a conditioning step and the subsequent three scans averaged. Cleaning scans were performed in-between each concentration to prevent any possible electrode fouling and improve reproducibility. These scans consisted of disconnecting WE1 and applying a typical CV 0.85 V to -0.2 V (versus Pt pseudo-reference) was applied to WE2 for 4 scans at a 50 mV/s scan rate. By applying these scan parameters to WE2, any potential fouling was minimised, ensuring a relatively constant electrode surface across all concentrations. WE1 was left disconnected to minimise unnecessary usage and therefore prolong the sensor lifespan.

Detection of free-chlorine with pH control in the presence of flow

Having optimised the free-chlorine pH control conditions within a channel, under quiescent conditions, the effect of flowrate was investigated. The microfluidic system was connected to a digitally programmable syringe pump to permit quantified flowrates through the channels. All CV parameters remained the same as the static conditions described above, except for the protonator bias, which was increased by 100 mV to 1.7V. This voltage increase was to drive a higher protonator current to offset

the hydrodynamic removal of some of the generated protons by flow which was observed to decrease the efficacy of the pH control. By generating extra protons, the pH was shifted back to the desired pH within the vicinity of the sensors; despite the effect of flow. Cleaning scans were again performed between each set of measurements.

System Design

Figure 1 (A) shows an exploded view of the Solidworks™ schematic for the microfluidic platform. The system consists of three separate parts; a hard base layer with a slot to hold the microchip as well as two pillars to ensure accurate alignment of the sensor chips. a middle gasket component, made of a soft flexible resin, which comes into conformal contact with the chip surface. this gasket had three microfluidic channels designed to align with the three sensor locations on a chip; as well as three inlet and outlet apertures to allow fluid flow. The third, hard, top layer was designed to apply a constant pressure to the middle gasket to prevent leakage. This constant pressure was ensured by locking the top component into place using two pegs to retain downwards pressure on the system, effectively sealing it.

Figure 1 (B) shows an optical micrograph plan view of the assembled system containing a chip, and three microfluidic channels in the correct orientation with the inlets and outlets for sample flow over the sensors. Tubes are omitted for clarity.

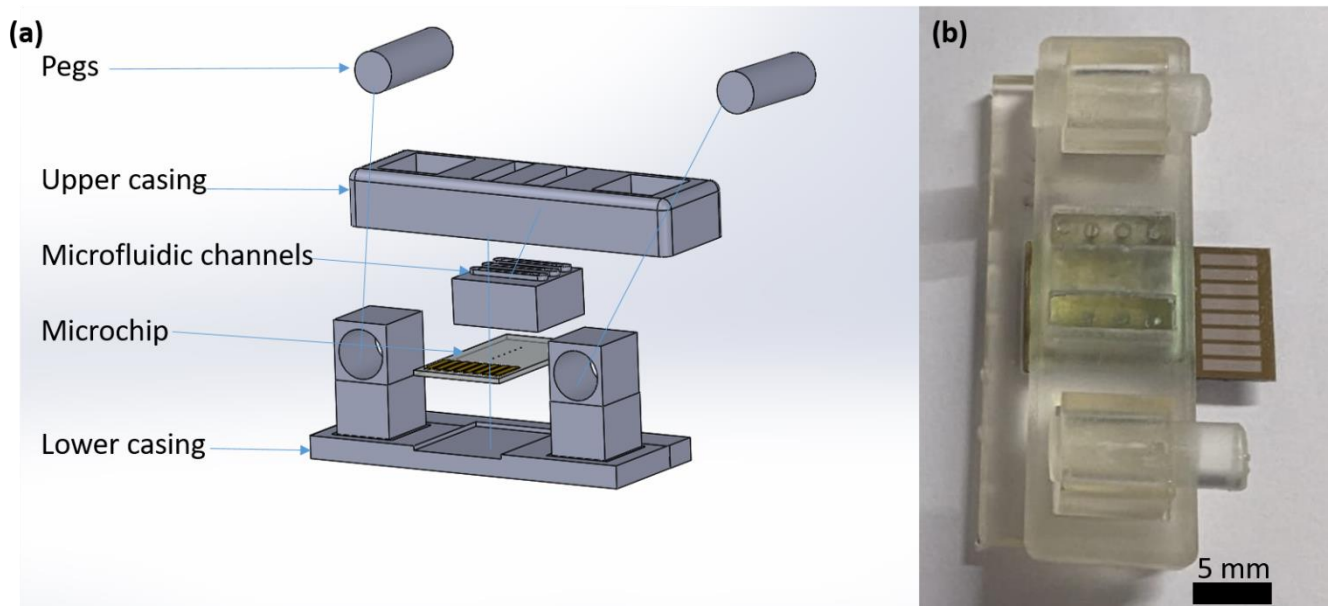

Figure 1 (A) Exploded view of the microfluidic platform and (B) top down view of assembled system with chip

Results and Discussion

Figure 2 (A) shows a typical COMSOL Multiphysics™ simulation of pH control in a region surrounding the interdigitated electrodes. Figure 2 (A) and (B) are set such that time is equal to 0.1s and 1s respectively, showing the overall array within the channel under static conditions. Their respective insets show the centremost generator-collector IDE. The longer duration in 2 (B) allowed more protons to be generated, lowering the localised pH when compared with 2 (A). The variation in pH across this duration (0.1-1 s) is also quite significant, with a pH of approximately 3.30 observed at 0.1s compared to a pH of 2.86 observed at 1s. The pH was measured at the surface of the leftmost electrode shown in the insets. This represents the pH present at the centre of the electrode array. Figure 2 (C) and (D) 0.1s and 1s, respectively, shows the same simulation conditions but with the addition of a fluid flow 200 µL/min introduced from left to right. When compared to their static counterparts, the diffusion profile has changed greatly, effectively removing the constraint of minimum domain size. The incorporation of flow compresses the diffusion profile of the protons towards the sensor surface, concentrating the protons nearby. The insets show the greatly decreased diffusion profile height around the electrode surface. The slightly lower decrease in pH, when compared to 2(A) and (B), is due to some of the generated protons being hydrodynamically removed thereby making the area less acidic. This can be

adjusted for by increasing the applied potential bias, which was undertaken in the subsequent experiments. The similarity between 2(C) and 2(D) suggests that the effect of flowrate on protonation does not intensify as time passes, but rather quickly reaches a constant value. In contrast to the quiescent simulations, the simulated pH at the leftmost electrodes are only marginally varied from 0.1s to 1s. The observed pH was 3.3 at 0.1s, changing to 3.2 at 1s, under flow conditions suggesting that under flow conditions the pH quickly reaches a set pH and maintains this value, therefore allowing local pH control under flow see insets Figure 3 (C) and (D)

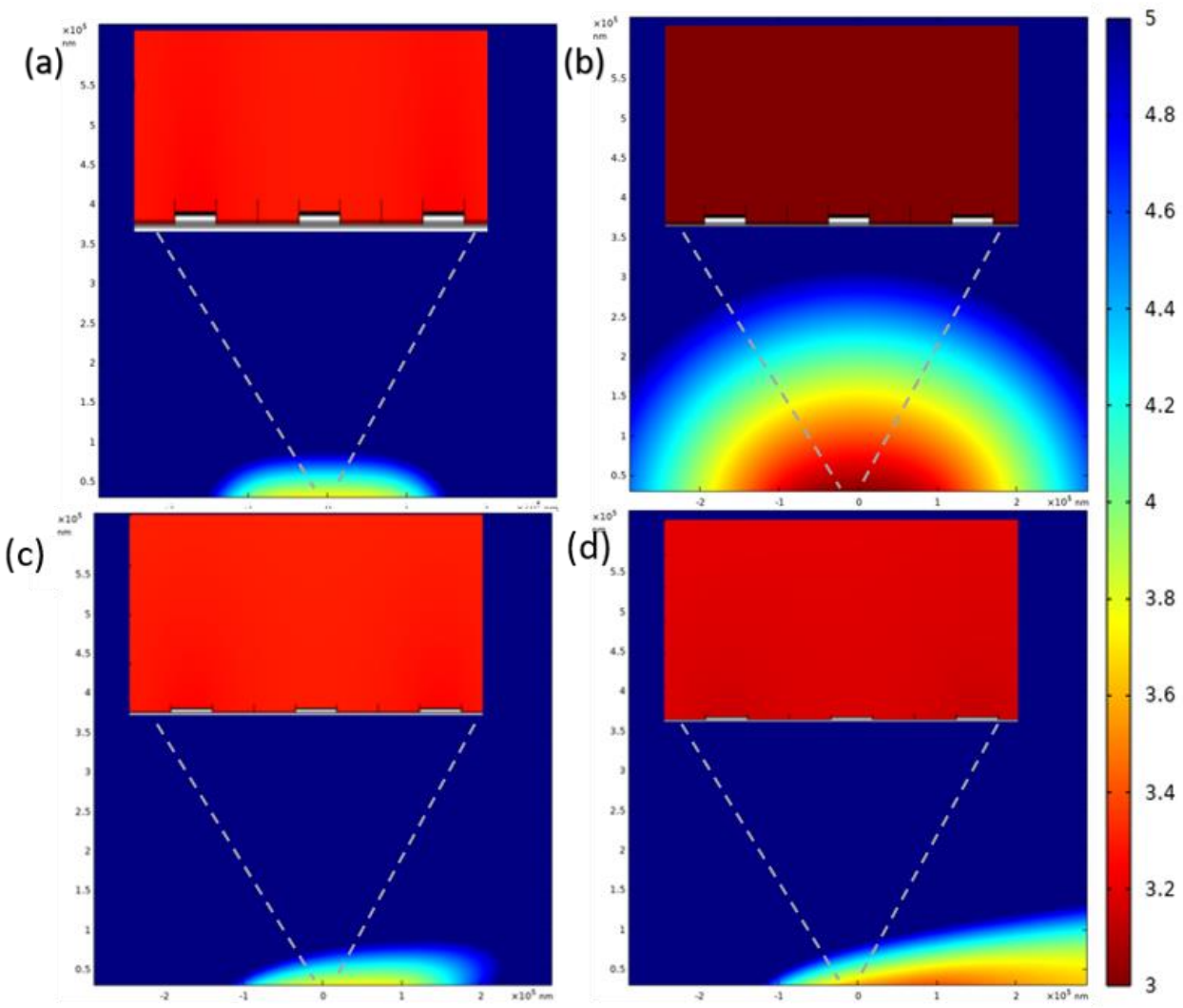

Figure 2: Comsol flow simulations of pH control with their respective insets varying time values. (A) Static conditions and time =0.1s (B) Static conditions and time = 1s (C) hydrodynamic conditions 200 uL/min flowrate with time =0.1s (D) 200 uL/min flowrate with time =1s

A silicon chip device consisting of three sensors and on-chip counter and reference electrodes is shown in Figure S1 (A) (Supp info) while S1 (B) (Supp info) shows an assembled microfluidic system, with the inlet and outlet tubes removed for clarity. Typically, inlet and outlet tubes would be connected to allow flow through the selected microchannel over a selected sensor. The distal ends contact pads of a microchip were connected to an external SD connector port, as shown. This allowed facile connection to an Autolab potentiostat.

Following optical microscopic inspection, sensors were electrochemically characterized using cyclic voltammetry (Vs on chip Pt pseudo reference), using 1.0 mM FCA as a redox probe. Figure 3 (A) shows typical CV scans performed in generator-collector mode, under various flowrates (10 - 200 uL/min). The generator was cycled from -0.15V to 0.45V while the collector was held at -0.15V. The generator comb oxidised the FCA to FCA^+. The FCA^+ species then diffused across the gap to the collector electrodes, where it was subsequently reduced back to FCA. This phenomenon is known as redox cycling and can be used to boost signals when using reversible redox molecules; as described by Seymour, et al. [32] The CV steady-state behavioural shape observed for the static FCA scan in **Error! Reference source not found.** (A): inset, arises from REDOX cycling as it surmounts the diffusion limited behaviour typically associated with transport of fresh analyte to the electrode. As a flowrate across an electrode surface is introduced and increased, the measured current response signals were observed to increase with increasing flow rate. However, the steady-state plateau of signal, typically associated with quiescent solutions, is replaced with an elongated current response at higher voltages with increasing flowrate. This is due to the addition of convection as a mode of mass transport, as opposed to the diffusion only conditions experienced in quiescent solutions. The convection allows for constant replenishment of fresh FCA at an electrode surface, thereby increasing the current response. Each voltammogram presented in Figure 3(A) is an average of three consecutive cycles for each flowrate: inset is a typical CV obtained under quiescent conditions.

Figure 3 (B) shows a linear relationship observed between the cubic root of flowrate and the measured current at 0.45V in **Error! Reference source not found.** (A). The cubic root of flow was selected as it was described previously within the Levich equation when considering the linearized Leveque approximation for the flowrate to a tubular electrode. Rees et al, showed this relationship to occur for multiple different electrode configurations, showing the relationship between limiting current and flowrate. Rees and Compton [73]

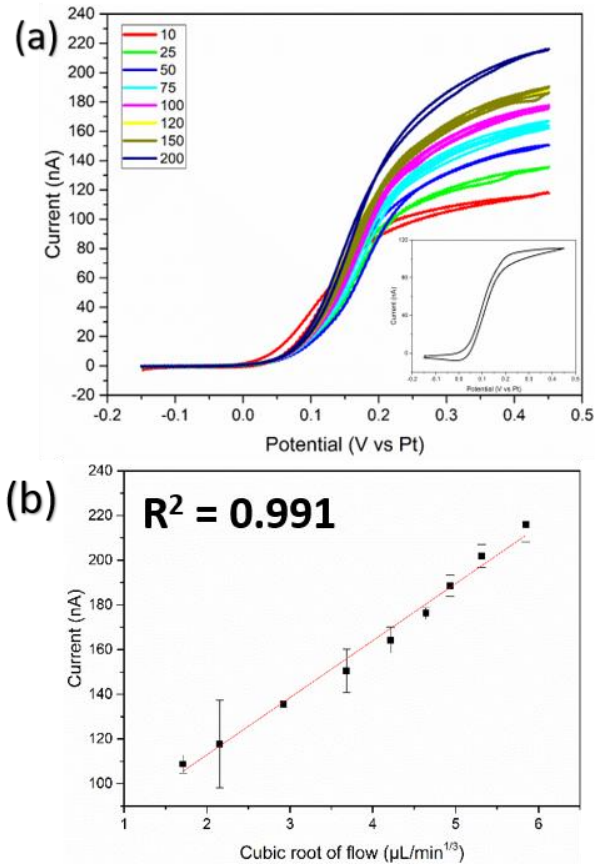

Figure 3:(a) Cyclic voltammograms of WE1 current for various flowrates in uL/min in 1mM FCA. Inset of (a) shows the static scan. (b) shows the cubic root of flowrate versus observed current for the flowrates in (a).

The generation and subsequent reduction of gold oxide was used as an indicator of pH, as shown previously by Seymour et al. [32] Chemical buffers in the pH range of 3 - 7.6 were characterised electrochemically to monitor the position of the reduction peak for each buffer, in both static and flow conditions (100 µL/min); Figure 4 (A) and (B) show these, respectively. Under both static and flowing conditions, little to no difference observed in the minima positions of the gold oxide reduction peaks. This suggests that flowing conditions has little effect on pH. This is further illustrated in Figure 4 (C) where two calibrations of gold oxide reduction potential minima versus pH for both hydrodynamic conditions are plotted and overlaid and exhibit very similar behaviour within the investigated pH range.

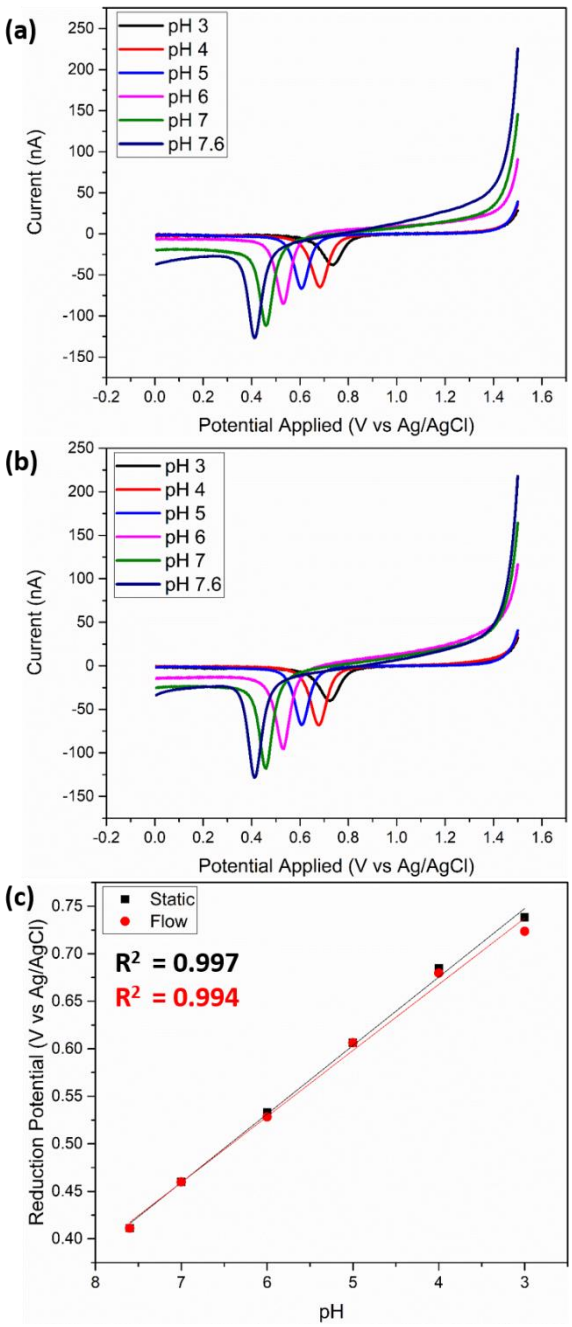

Figure 4:(a) Chemically adjusted pH buffers showing the oxide reduction peak in static conditions, (b) in flow conditions 100 µL/min and (c) the calibration of both static and flow

Electrochemical-based pH control was then investigated in both static and flowing conditions, using a PB solution with an initial pH of 7.4. The effect of flowrate on electrochemical pH control has hitherto not been demonstrated in the literature. The PB buffer solution was electrochemically acidified using various protonator potentials and the CVs was observed and recorded under both static and flow (100 µL/min) conditions. The reduction peak minima versus pronator potential applied were again used as an indicator of pH and are plotted in Figure 5 (A) and (B), respectively. The insets of these figures are

the respective calibrations. Unlike Figure 2 there is a visible decrease in the shift of the reduction peak minima observed for a set protonator potential when a flow is introduced. The lower anodic shift observed under flow conditions, suggests less efficient protonation i.e., leading to less acidic conditions through removal of protons by hydrodynamic forces. This can be observed more clearly in the respective calibrations plots of pH versus protonator potential for static and flow, in 5 (C). The observed pH under flow conditions is notably less acidic (lower anodic shift) for each potential, confirming less efficient protonation. We attribute this reduced acidification to the protons being generated at the protonator being washed away by the flowing liquid. This effect can be remediated by increasing the applied potential and producing additional protons as shown in Figures 2 (C) and (D).

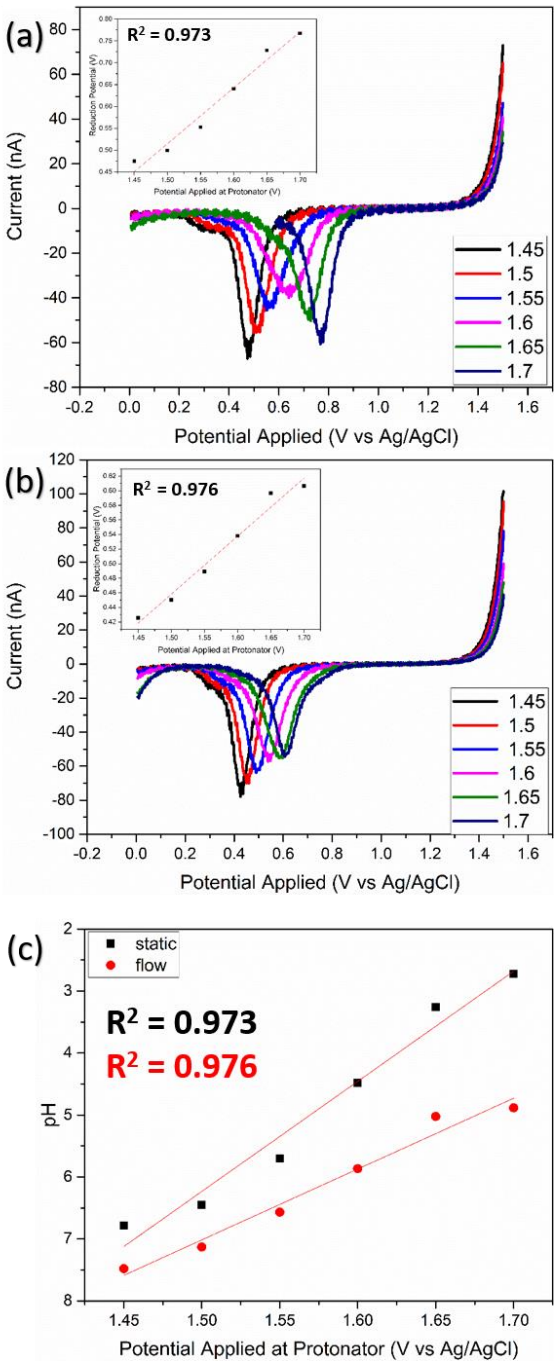

Figure 5:(a) Electrochemically adjusted pH buffer showing the oxide reduction peak in static conditions, inset calibration (b) in flow conditions (100 $\mu L/min$), inset calibration, and (c) the calibration of both static and flow protonator potential versus pH observed

Figure 6 (A) shows typical CV scans in ADW. When the pH control is off (black line) the oxide reduction minimum occurs at a potential ~ 0.2 V vs Pt. However, when the pH control is activated (red line) the gold oxide reduction shifts anodically to approximately ~0.6 V. This acidification is a result of biasing the second working electrode at ~1.5 V with the subsequent production of protons.

To compensate for less efficient acidification under flow conditions described above, application of a higher potential bias, by 100 mV at WE2, generates more protons, effectively replacing those washed away. It was observed that application of this slightly higher voltage (1.6 V), the position of the reduction peas minima remained constant for measured flow rates up to 200 μL/min. Data preparation in Figure 6 (B) involved undertaking an initial cleaning/conditioning scan and then averaging the subsequent three CVs for each flow rate. To eliminate any effects due to capacitive current a baseline for normalisation was chosen to be the 25 μL/min data, in the non-Faradaic region, i.e., approximately 0.3 V. This current was then set as the baseline and subtracted from all other current values within those scans. As the flowrate increases, the shift in location of the oxide peak is negligible for this range of flowrates, consistently remaining at ~ 0.7 V. This confirms that within the pH range selected, the electrochemical pH is still demonstrating acidic behaviour, and the washing away effect of protons eliminated. Flowrates higher than 200 μL/min were not explored due to the potential for tubes to pop out of the holder during experiments.

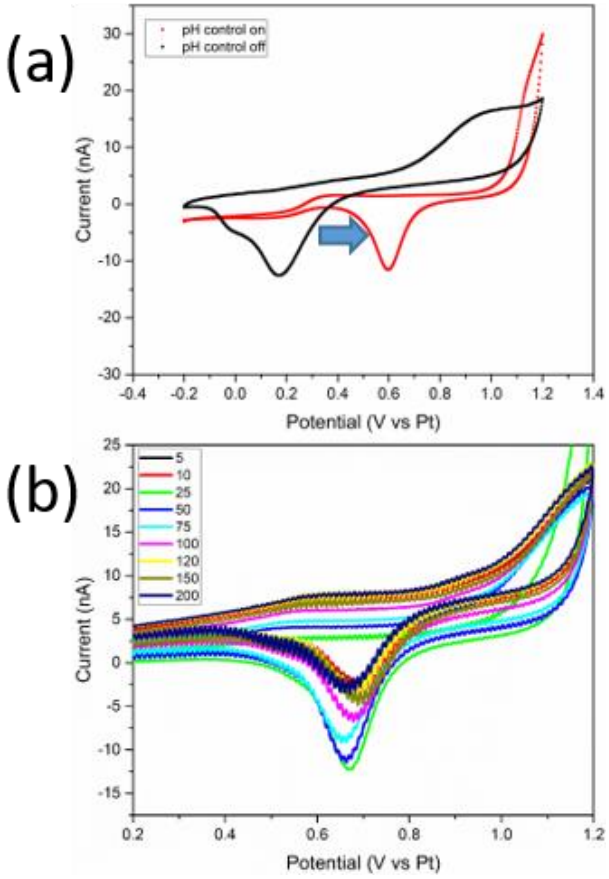

Figure 6:(a) CVs showing both no pH control and pH control for gold oxide generation and reduction. ((b) Gold oxide oxide detection under various flow rates (5 – 200 µL/min). the gold oxide reduction peak minima area clearly visible at ~0.67 V

Once the effects of flowrate on desired pH had been compensated for, electrochemical analysis was then undertaken. Hypochlorous acid was selected as an analyte of interest due to its importance is water sterilisation. [32] A stock solution of 5.3 ppm was prepared and used to assess the impacts of flowrate.

For each flowrate, the pH was electrochemically controlled by applying a potential bias of 1.65V to the protonator. This allowed the local pH to be set to ~5. This pH is lower than pH 6 the value where all free-chlorine is converted to hypochlorous acid; see Fig S2. The effect of this pH control can be seen in Fig S3 where no hypochlorous acid was detected in a solution of 5ppm NaOCl without pH control enabled whereas hypochlorous acid was readily detected once pH control was enabled. Once the parameters had been optimised, CVs were carried out using quantifiable flowrates, using the calibrated digital syringe pump. The signal-boosting effect of flowrate is clearly visible with an increase in

measured current observed with increasing flowrate in clearly observed in Figure 7 (A). The relationship between flowrate and the measured current of hypochlorous acid concentrations was highly linear and again seen to be proportional to the cubic root of flow; inset of Figure 7 (A). Figure 7 (B) shows the detection of hypochlorous acid under quiescent (black line) and high flow rate conditions (red line) ~10 mL/min obtained by manually pumping the system with a syringe. Under this high flow condition, the experimental window was required to be broadened, -0.2V to 0.85V, in order to observe the hypochlorous acid detection. All other experimental parameters remained unadjusted. Electrochemical activity is present in both flow conditions; however, the flow enhancement dwarfs the quiescent scan current. The inset in Figure 7 (B) shows the electrochemical activity of the quiescent scan. This higher flowrate was observed to amplify the chlorine detection, with a near 30-fold increase in signal (5 nA to 130 nA).

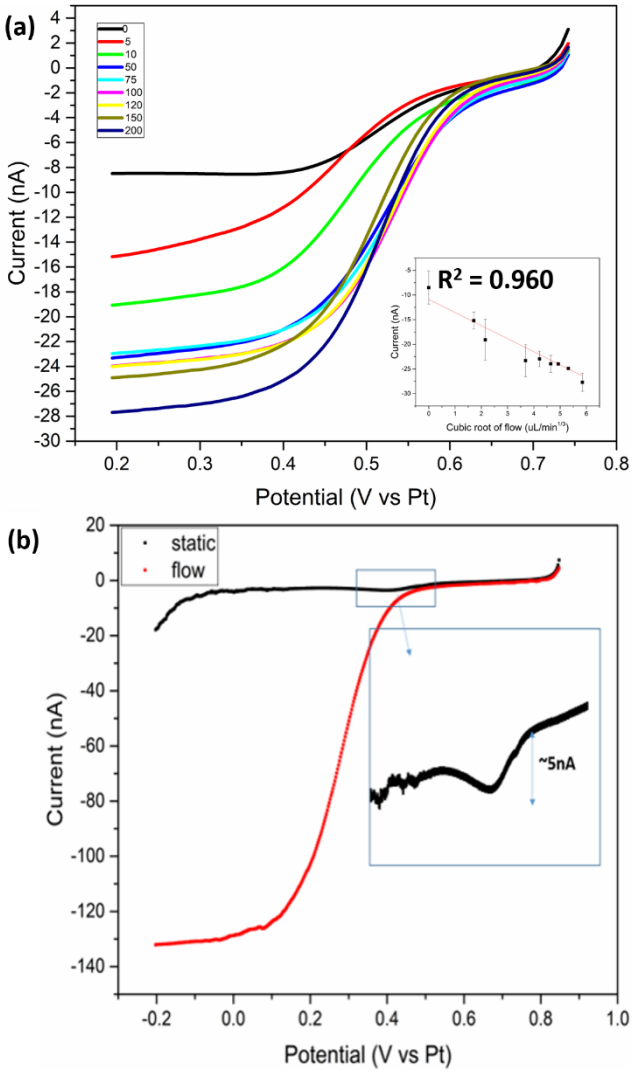

Figure 7: (a) Hypochlorous acid detection under various flowrates. Inset: the cubic root of the flowrates shown in (A) vs current. (b) Hypochlorous acid detection in static and high flow conditions. Inset shows the activity of static scan in greater detail.

Conclusion

We have shown a simulation and experimental study of electrochemical pH control under both static and hydrodynamic conditions at interdigitated gold microband arrays. The finite element simulations demonstrated the feasibility of performing electrochemical pH control under flow conditions, which was then validated experimentally. Detection of hypochlorous acid under various flowrates was performed. The high flowrate did not cause the pH to drift outside of the optimum pH window for hypochlorous acid detection, however with future detection of other molecules the pH window could be narrower. The decrease in the pH control by flow can be compensated for with an increase in potential

bias, as shown previously in Figure 4 (B) and (C). This suggests that there is great potential for future work on the coupling of these phenomena.

Acknowledgements

This publication has emanated from research supported by a research grant from Science Foundation Ireland and the Department of Agriculture, Food and Marine on behalf of the Government of Ireland under the Grant 16/RC/3835 (VistaMilk) and also under Department of Agriculture, Food and the Marine (DAFM) under the grant number 17/RD/US-ROI/56.

References

1. Vailshery, L. S. IOT connected devices worldwide 2019-2030. https://www.statista.com/statistics/1183457/iot-connected-devices-worldwide/ (accessed 30 March).
2. Cesar Souza Machado, C.; da Silveira Petruci, J. F.; G. Silva, S., An IoT optical sensor for photometric determination of oxalate in infusions. *Microchemical Journal* **2021,** *168*, 106466.
3. Trevathan, J.; Read, W.; Sattar, A., Implementation and Calibration of an IoT Light Attenuation Turbidity Sensor. *Internet of Things* **2022,** *19*, 100576.
4. Yoo, M.; Bhuiyan, N. H.; Uddin, M. J.; Shim, J. S., An IoT-based smart optical platform for colorimetric analyzing multiple samples of biomarkers. *Sensors and Actuators A: Physical* **2023,** *353*, 114228.
5. Zhao, S.; Zhang, H. B.; Luo, J. Q.; Wang, Q. W.; Xu, B.; Hong, S.; Yu, Z. Z., Highly Electrically Conductive Three-Dimensional Ti3C2Tx MXene/Reduced Graphene Oxide Hybrid Aerogels with Excellent Electromagnetic Interference Shielding Performances. *ACS Nano* **2018,** *12* (11), 11193-11202.
6. Kim, S. J.; Koh, H. J.; Ren, C. E.; Kwon, O.; Maleski, K.; Cho, S. Y.; Anasori, B.; Kim, C. K.; Choi, Y. K.; Kim, J.; Gogotsi, Y.; Jung, H. T., Metallic Ti3C2Tx MXene Gas Sensors with Ultrahigh Signal-to-Noise Ratio. *ACS Nano* **2018,** *12* (2), 986-993.
7. Xu, B.; Zhu, M.; Zhang, W.; Zhen, X.; Pei, Z.; Xue, Q.; Zhi, C.; Shi, P., Ultrathin MXene-Micropattern-Based Field-Effect Transistor for Probing Neural Activity. *Advanced Materials* **2016,** *28* (17), 3333-3339.
8. Brezolin, A. N.; Martinazzo, J.; Steffens, J.; Steffens, C., Polyaniline–graphene oxide nanocomposite microelectromechanical sensor for stink bugs pheromone detection. *Sensors and Actuators B: Chemical* **2020,** *305*, 127426.
9. Ma, W.; Jiang, Y.; Hu, J.; Jiang, L.; Zhang, T.; Zhang, T., Microelectromechanical system-based, high-finesse, optical fiber Fabry–Perot interferometric pressure sensors. *Sensors and Actuators A: Physical* **2020,** *302*, 111795.
10. Haronian, D.; MacDonald, N. C., A microelectromechanics-based frequency-signature sensor. *Sensors and Actuators A: Physical* **1996,** *53* (1), 288-298.

11. Mohanraj, J.; Durgalakshmi, D.; Rakkesh, R. A.; Balakumar, S.; Rajendran, S.; Karimi-Maleh, H., Facile synthesis of paper based graphene electrodes for point of care devices: A double stranded DNA (dsDNA) biosensor. *Journal of Colloid and Interface Science* **2020,** *566*, 463-472.
12. Lee, H.; Song, C.; Hong, Y. S.; Kim, M. S.; Cho, H. R.; Kang, T.; Shin, K.; Choi, S. H.; Hyeon, T.; Kim, D. H., Wearable/disposable sweat-based glucose monitoring device with multistage transdermal drug delivery module. *Science Advances* **2017,** *3* (3).
13. Yakoh, A.; Pimpitak, U.; Rengpipat, S.; Hirankarn, N.; Chailapakul, O.; Chaiyo, S., Paper-based electrochemical biosensor for diagnosing COVID-19: Detection of SARS-CoV-2 antibodies and antigen. *Biosensors and Bioelectronics* **2021,** *176*.
14. Chaiyo, S.; Mehmeti, E.; Siangproh, W.; Hoang, T. L.; Nguyen, H. P.; Chailapakul, O.; Kalcher, K., Non-enzymatic electrochemical detection of glucose with a disposable paper-based sensor using a cobalt phthalocyanine–ionic liquid–graphene composite. *Biosensors and Bioelectronics* **2018,** *102*, 113-120.
15. Zhang, Y.; Qin, Y.; Jiao, L.; Wang, H.; Wu, Z.; Wei, X.; Wu, Y.; Wu, N.; Hu, L.; Zhong, H.; Gu, W.; Zhu, C., Atomically thin bismuthene nanosheets for sensitive electrochemical determination of heavy metal ions. *Anal Chim Acta* **2022,** *1235*, 340510.
16. Daly, R.; Narayan, T.; Shao, H.; O'Riordan, A.; Lovera, P. Platinum-Based Interdigitated Micro-Electrode Arrays for Reagent-Free Detection of Copper *Sensors* [Online], 2021. https://mdpi-res.com/d_attachment/sensors/sensors-21-03544/article_deploy/sensors-21-03544-v2.pdf?version=1621501310.
17. Zhang, M.; Guo, W., Simultaneous electrochemical detection of multiple heavy metal ions in milk based on silica-modified magnetic nanoparticles. *Food Chem* **2023,** *406*, 135034.
18. Ahmed, A.; Rushworth, J. V.; Hirst, N. A.; Millner, P. A., Biosensors for whole-cell bacterial detection. *Clinical Microbiology Reviews* **2014,** *27* (3), 631-646.
19. Abbaspour, A.; Norouz-Sarvestani, F.; Noori, A.; Soltani, N., Aptamer-conjugated silver nanoparticles for electrochemical dual-aptamer-based sandwich detection of staphylococcus aureus. *Biosensors and Bioelectronics* **2015,** *68*, 149-155.
20. Wasiewska, L. A.; Diaz, F. G.; Shao, H.; Burgess, C. M.; Duffy, G.; O'Riordan, A., Highly sensitive electrochemical sensor for the detection of Shiga toxin-producing E. coli (STEC) using interdigitated micro-electrodes selectively modified with a chitosan-gold nanocomposite. *Electrochim Acta* **2022,** *426*.
21. Bagheri, H.; Hajian, A.; Rezaei, M.; Shirzadmehr, A., Composite of Cu metal nanoparticles-multiwall carbon nanotubes-reduced graphene oxide as a novel and high performance platform of the electrochemical sensor for simultaneous determination of nitrite and nitrate. *Journal of Hazardous Materials* **2017,** *324*, 762-772.
22. Patella, B.; Russo, R. R.; O'Riordan, A.; Aiello, G.; Sunseri, C.; Inguanta, R., Copper nanowire array as highly selective electrochemical sensor of nitrate ions in water. *Talanta* **2021,** *221*.
23. Ali, M. A.; Jiang, H.; Mahal, N. K.; Weber, R. J.; Kumar, R.; Castellano, M. J.; Dong, L., Microfluidic impedimetric sensor for soil nitrate detection using graphene oxide and conductive nanofibers enabled sensing interface. *Sensors and Actuators, B: Chemical* **2017,** *239*, 1289-1299.
24. Patella, B.; Parisi, A.; Moukri, N.; Gitto, F.; Busacca, A.; Aiello, G.; Russo, M.; O'Riordan, A.; Inguanta, R., Phosphate ions detection by using an electrochemical sensor based on laser-scribed graphene oxide on paper. *Electrochim Acta* **2023,** *461*.
25. Dodds, L.; King, W.; Woolcott, C.; Pole, J., Trihalomethanes in public water supplies and adverse birth outcomes. *Epidemiology* **1999**, 233-237.
26. Shafiee, M.; Reza, M.; Taghavi, L., Health effects of trihalomethanes as chlorinated disinfection by products: A review article. *World Academy of Science, Engineering and Technology* **2012,** *68*, 2090-2096.
27. de Castro Medeiros, L.; de Alencar, F. L. S.; Navoni, J. A.; de Araujo, A. L. C.; do Amaral, V. S., Toxicological aspects of trihalomethanes: a systematic review. *Environmental Science and Pollution Research* **2019,** *26*, 5316-5332.

28. Westerlund, J.; Bryngelsson, I.-L.; Löfstedt, H.; Eriksson, K.; Westberg, H.; Graff, P., Occupational exposure to trichloramine and trihalomethanes: adverse health effects among personnel in habilitation and rehabilitation swimming pools. *Journal of Occupational and Environmental Hygiene* **2019,** *16* (1), 78-88.
29. Chiang, Y.-T.; Chou, S.-C.; Sun, B.-Y.; Wu, P.-W., A conductive silver membrane for electrochemical detection of free chlorine in aqueous solution. *Sensors and Actuators B: Chemical* **2021,** *348*, 130724.
30. Kabir, H.; Ma, P. Y.; Renn, N.; Nicholas, N. W.; Cheng, I. F., Electrochemical determination of free chlorine on pseudo-graphite electrode. *Talanta* **2019,** *205*, 120101.
31. Jović, M.; Cortés-Salazar, F.; Lesch, A.; Amstutz, V.; Bi, H.; Girault, H. H., Electrochemical detection of free chlorine at inkjet printed silver electrodes. *Journal of Electroanalytical Chemistry* **2015,** *756*, 171-178.
32. Seymour, I.; O'Sullivan, B.; Lovera, P.; Rohan, J. F.; O'Riordan, A., Electrochemical detection of free-chlorine in Water samples facilitated by in-situ pH control using interdigitated microelectrodes. *Sensors and Actuators B-Chemical* **2020,** *325*, 128774.
33. Wilder, L. M.; Thompson, J. R.; Crooks, R. M., Electrochemical pH regulation in droplet microfluidics. *Lab Chip* **2022,** *22* (3), 632-640.
34. Dickinson, E. J. F.; Ekstrom, H.; Fontes, E., COMSOL Multiphysics (R) : Finite element software for electrochemical analysis. A mini-review. *Electrochemistry Communications* **2014,** *40*, 71-74.
35. Kaffash, A.; Rostami, K.; Zare, H. R., Modeling of an electrochemical nanobiosensor in COMSOL Multiphysics to determine phenol in the presence of horseradish peroxidase enzyme. *Enzyme Microb Technol* **2019,** *121*, 23-28.
36. O'Sullivan, B.; O'Sullivan, S.; Narayan, T.; Shao, H.; Patella, B.; Seymour, I.; Inguanta, R.; O'Riordan, A., A direct comparison of 2D versus 3D diffusion analysis at nanowire electrodes: A finite element analysis and experimental study. *Electrochim Acta* **2022,** *408*, 139890.
37. O'Sullivan, B.; Patella, B.; Daly, R.; Seymour, I.; Robinson, C.; Lovera, P.; Rohan, J.; Inguanta, R.; O'Riordan, A., A simulation and experimental study of electrochemical pH control at gold interdigitated electrode arrays. *Electrochim Acta* **2021,** *395*, 139113.
38. Belmonte, I.; White, R. J., 3-D printed microfluidics for rapid prototyping and testing of electrochemical, aptamer-based sensor devices under flow conditions. *Analytica Chimica Acta* **2022,** *1192*, 339377.
39. Ko, E.; Tran, V.-K.; Geng, Y.; Chung, W. S.; Park, C. H.; Kim, M. K.; Jin, G. H.; Seong, G. H., Continuous electrochemical detection of hydrogen peroxide by Au-Ag bimetallic nanoparticles in microfluidic devices. *Journal of Electroanalytical Chemistry* **2017,** *792*, 72-78.
40. Jofre, C. F.; Regiart, M.; Fernández-Baldo, M. A.; Bertotti, M.; Raba, J.; Messina, G. A., Electrochemical microfluidic immunosensor based on TES-AuNPs@Fe3O4 and CMK-8 for IgG anti-Toxocara canis determination. *Analytica Chimica Acta* **2020,** *1096*, 120-129.
41. Hernández-Rodríguez, J. F.; Rojas, D.; Escarpa, A., Rapid and cost-effective benchtop microfabrication of disposable carbon-based electrochemical microfluidic devices. *Sensors and Actuators B: Chemical* **2020,** *324*, 128679.
42. Steegstra, P.; Ahlberg, E., In situ pH measurements with hydrous iridium oxide in a rotating ring disc configuration. *Journal of Electroanalytical Chemistry* **2012,** *685*, 1-7.
43. Vesztergom, S.; Ujvári, M.; Láng, G. G., Dual cyclic voltammetry with rotating ring–disk electrodes. *Electrochim Acta* **2013,** *110*, 49-55.
44. Zimer, A. M.; Medina da Silva, M.; Machado, E. G.; Varela, H.; Mascaro, L. H.; Pereira, E. C., Development of a versatile rotating ring-disc electrode for in situ pH measurements. *Analytica Chimica Acta* **2015,** *897*, 17-23.
45. Filimonenkov, I. S.; Istomin, S. Y.; Antipov, E. V.; Tsirlina, G. A.; Savinova, E. R., Rotating ring-disk electrode as a quantitative tool for the investigation of the oxygen evolution reaction. *Electrochim Acta* **2018,** *286*, 304-312.

46. Ramanujam, A.; Neyhouse, B.; Keogh, R. A.; Muthuvel, M.; Carroll, R. K.; Botte, G. G., Rapid electrochemical detection of Escherichia coli using nickel oxidation reaction on a rotating disk electrode. *Chemical Engineering Journal* **2021,** *411*, 128453.
47. Xia, Y.; Whitesides, G. M., SOFT LITHOGRAPHY. *Annual Review of Materials Science* **1998,** *28* (1), 153-184.
48. Han, K. N.; Li, C. A.; Bui, M. P. N.; Seong, G. H., Patterning of single-walled carbon nanotube films on flexible, transparent plastic substrates. *Langmuir* **2010,** *26* (1), 598-602.
49. Sun, X.; Chen, W.; Zhang, B., A portable microfluidic device integrated with electrochemical sensing platform for detection of multiple binders in ancient wall paintings. *Analytica Chimica Acta* **2023,** *1275*, 341562.
50. Cao, J.-T.; Zhu, Y.-D.; Rana, R. K.; Zhu, J.-J., Microfluidic chip integrated with flexible PDMS-based electrochemical cytosensor for dynamic analysis of drug-induced apoptosis on HeLa cells. *Biosensors and Bioelectronics* **2014,** *51*, 97-102.
51. Zhang, C.; Shi, D.; Li, X.; Yuan, J., Microfluidic electrochemical magnetoimmunosensor for ultrasensitive detection of interleukin-6 based on hybrid of AuNPs and graphene. *Talanta* **2022,** *240*, 123173.
52. Deal, B. E.; Fleming, P. J.; Castro, P. L., Electrical Properties of Vapor-Deposited Silicon Nitride and Silicon Oxide Films on Silicon. *Journal of The Electrochemical Society* **1968,** *115* (3), 300.
53. Zhang, J. X. J.; Hoshino, K., Chapter 2 - Fundamentals of nano/microfabrication and scale effect. In *Molecular Sensors and Nanodevices (Second Edition)*, Zhang, J. X. J.; Hoshino, K., Eds. Academic Press: 2019; pp 43-111.
54. Bartholomeusz, D. A.; Boutte, R. W.; Andrade, J. D., Xurography: rapid prototyping of microstructures using a cutting plotter. *Journal of Microelectromechanical Systems* **2005,** *14* (6), 1364-1374.
55. Kim, S.-W.; Kang, K.-N.; Min, J.-W.; Jang, J.-H., Plotter-assisted integration of wearable all-solid-state micro-supercapacitors. *Nano Energy* **2018,** *50*, 410-416.
56. Bishop, G. W.; Satterwhite-Warden, J. E.; Kadimisetty, K.; Rusling, J. F., 3D-printed bioanalytical devices. *Nanotechnology* **2016,** *27* (28).
57. Zhang, Y.; Ge, S.; Yu, J., Chemical and biochemical analysis on lab-on-a-chip devices fabricated using three-dimensional printing. *TrAC Trends in Analytical Chemistry* **2016,** *85*, 166-180.
58. Au, A. K.; Huynh, W.; Horowitz, L. F.; Folch, A., 3D-Printed Microfluidics. *Angew. Chem. Int. Ed.* **2016,** *55* (12), 3862-3881.
59. Bhattacharjee, N.; Urrios, A.; Kang, S.; Folch, A., The upcoming 3D-printing revolution in microfluidics. *Lab Chip* **2016,** *16* (10), 1720-1742.
60. Gross, B.; Lockwood, S. Y.; Spence, D. M., Recent advances in analytical chemistry by 3D printing. *Anal. Chem.* **2017,** *89* (1), 57-70.
61. Wang, L.; Pumera, M., Recent advances of 3D printing in analytical chemistry: Focus on microfluidic, separation, and extraction devices. *TrAC Trends Anal. Chem.* **2021,** *135*.
62. Adamski, K.; Kawa, B.; Walczak, R. 3D Printed Flowmeter Based on Venturi Effect with Integrated Pressure Sensors *Proceedings* [Online], 2018.
63. Wolterink, G.; Umrani, A.; Schouten, M.; Sanders, R.; Krijnen, G. In *3D-Printed Calorimetric Flow Sensor*, 2020 IEEE SENSORS, 25-28 Oct. 2020; 2020; pp 1-4.
64. Khosravani, M. R.; Reinicke, T., 3D-printed sensors: Current progress and future challenges. *Sensors and Actuators A: Physical* **2020,** *305*, 111916.
65. Radovanović, M.; Ilić, M.; Pastor, K.; Ačanski, M.; Panić, S.; Srdić, V. V.; Randjelović, D.; Kojić, T.; Stojanović, G. M., Rapid detection of olive oil blends using a paper-based portable microfluidic platform. *Food Control* **2021,** *124*, 107888.
66. Xiao, N.; Wu, R.; Huang, J. J.; Selvaganapathy, P. R., Development of a xurographically fabricated miniaturized low-cost, high-performance microbial fuel cell and its application for sensing biological oxygen demand. *Sensors and Actuators B: Chemical* **2020,** *304*, 127432.

67. Gosset, A.; Durrieu, C.; Renaud, L.; Deman, A.-L.; Barbe, P.; Bayard, R.; Chateaux, J.-F., Xurography-based microfluidic algal biosensor and dedicated portable measurement station for online monitoring of urban polluted samples. *Biosensors and Bioelectronics* **2018,** *117*, 669-677.
68. Swensen, J. S.; Xiao, Y.; Ferguson, B. S.; Lubin, A. A.; Lai, R. Y.; Heeger, A. J.; Plaxco, K. W.; Soh, H. T., Continuous, real-time monitoring of cocaine in undiluted blood serum via a microfluidic, electrochemical aptamer-based sensor. *J. Am. Chem. Soc.* **2009,** *131* (12), 4262-4266.
69. Speller, N. C.; Morbioli, G. G.; Cato, M. E.; Cantrell, T. P.; Leydon, E. M.; Schmidt, B. E.; Stockton, A. M., Cutting edge microfluidics: Xurography and a microwave. *Sensors and Actuators B: Chemical* **2019,** *291*, 250-256.
70. Dawson, K.; Wahl, A.; Barry, S.; Barrett, C.; Sassiat, N.; Quinn, A. J.; O'Riordan, A., Fully integrated on-chip nano-electrochemical devices for electroanalytical applications. *Electrochim Acta* **2014,** *115*, 239-246.
71. Seymour, I.; Narayan, T.; Creedon, N.; Kennedy, K.; Murphy, A.; Sayers, R.; Kennedy, E.; O'Connell, I.; Rohan, J. F.; O'Riordan, A. Advanced Solid State Nano-Electrochemical Sensors and System for Agri 4.0 Applications *Sensors* [Online], 2021.
72. Lee, S. H.; Rasaiah, J. C., Proton transfer and the mobilities of the H+ and OH- ions from studies of a dissociating model for water. *J Chem Phys* **2011,** *135* (12).
73. Rees, N. V.; Compton, R. G., Hydrodynamic microelectrode voltammetry. *Russian Journal of Electrochemistry* **2008,** *44* (4), 368-389.